

O-anion transport measured in several $R_2M_2O_7$ pyrochlores using perturbed-angular-correlation spectroscopy

Gary L. Catchen

Department of Nuclear Engineering and Electronic Materials and Processing Research Laboratory, The Pennsylvania State University, University Park, Pennsylvania 16802

Todd M. Rearick

Department of Engineering Science and Mechanics and Electronic Materials and Processing Research Laboratory, The Pennsylvania State University, University Park, Pennsylvania 16802

(Received 11 May 1995)

We have used perturbed-angular-correlation (PAC) spectroscopy to measure static and fluctuating electric-field gradients (EFG's) at the M sites in the pyrochlore ceramic materials, $R_2M_2O_7$ ($R = \text{Nd, Sm, Eu, and Gd}$; $M = \text{Zr and Hf}$). Samples were doped with a small concentration of $^{181}\text{Hf} \rightarrow ^{181}\text{Ta}$ PAC probe ions, and the M -site nuclear electric-quadrupole interactions were observed primarily at elevated temperatures that ranged up to approximately 1300 K. At temperatures below several hundred degrees, the perturbation functions for the Sm-, Eu-, and Gd-containing compounds show broadened lines that indicate primarily the presence of static, disordered O ions. At somewhat higher temperatures, the perturbation functions show attenuated lines that fluctuating EFG's produce, which arise from the hopping motion of O ions. At very high temperatures, the perturbation functions show sharp lines, which have shapes that reflect the presence of axial symmetry, and these line shapes indicate that the EFG fluctuation rates have increased to the motional-narrowing limit. Analysis of the attenuation rates, which were measured in the fast fluctuation regime, give activation energies that range from ≈ 0.17 eV to ≈ 0.32 eV. We associate these activation energies with the electrostatic barriers that O ions encounter when they jump to a vacant site. In contradistinction, the measurements on $\text{Nd}_2\text{Zr}_2\text{O}_7$ show sharp lines over the entire temperature range. This result indicates that the O ions are ordered in the $\text{Nd}_2\text{Zr}_2\text{O}_7$ crystal and that low-temperature kinetic pathways to disordered structures are not accessible to the O ions. The magnitudes of the measured activation energies are not consistent with the results of theoretical calculations and with electrical-conductivity-measured energies reported earlier. Thus, the O-anion transport effects, which we used PAC spectroscopy to measure, provide new benchmarks for future theoretical calculations, and these effects suggest that pyrochlores such as $\text{Gd}_2\text{Zr}_2\text{O}_7$ may become the basis for compounds from which new types of ionic-conducting materials could be developed.

I. INTRODUCTION

Investigating O-anion transport in binary and ternary metal-oxide crystals could potentially lead to new materials that could be used in a variety of high-temperature applications, which would make use of the ionic-conductivity property of these crystals. Moreover, the theoretical description of defect transport, for example, the calculation of potential-barrier heights and defect formation energies is difficult to test, because a detailed, reliable base of experimental information is not available. Using measurements of bulk, macroscopic properties such as electrical conductivity to obtain, for example, barriers to O-anion hopping is not reliable, because the derived barriers can represent averages over many types of microscopic processes. This situation is especially true for conductivity measurements that are performed on ceramics.

To overcome the limited applicability of conventional, macroscopic measurements, several groups of investigators have been developing perturbed-angular-correlation (PAC) spectroscopy to obtain more detailed microscopic information about an ionic transport in metal-oxide crystals. The PAC method is based on substituting a small number of radioactive probe ions into specific sites in the

crystal of interest. The local environment near the radioactive probe nucleus affects the subsequent decays of these nuclei in a subtle but measurable way, which we describe in more detail below. In 1982, Baudry, Boyer, and deOliveira¹ reported an investigation of O-anion transport in several heavily doped binary oxides that included Ca- and Y-stabilized ZrO_2 , which they carried out using $^{181}\text{Hf} \rightarrow ^{181}\text{Ta}$ PAC spectroscopy. Gardner *et al.*² extended the investigations using both $^{181}\text{Hf} \rightarrow ^{181}\text{Ta}$ and $^{111}\text{In} \rightarrow ^{111}\text{Cd}$ PAC spectroscopy, and they³ used the $^{111}\text{In} \rightarrow ^{111}\text{Cd}$ PAC probe to investigate defect trapping and O-anion transport in CeO_2 .

Generally, the investigations of alloys of ZrO_2 have involved primarily heavily doped crystals that have disordered cation sublattices and large O-vacancy concentrations.^{1,2} Because the chemistry of the $^{111}\text{In} \rightarrow ^{111}\text{Cd}$ probe ion differs from that of the Ce ion in CeO_2 , the corresponding measurements involved the complicating effects of probe-defect interactions in addition to the effects of O-anion hopping, which relatively small O-vacancy concentration facilitate in CeO_2 .³ The experimental objective of this investigation has been to observe the effects of O-anion transport in ternary metal-oxide crystals, namely, the $R_2M_2O_7$ pyrochlores that have ordered cation

sublattices, in which the probe ion, $^{181}\text{Hf} \rightarrow ^{181}\text{Ta}$, has essentially the same chemistry as the indigenous ions, Zr^{4+} and Hf^{4+} , for which it is substituted. The advantages of this approach are twofold. First, because these pyrochlores are not heavily doped, their crystal structures are well defined and ordered, so that any theoretical calculations that would be performed subsequently would not need to take into account the effects of cation disorder. Second, as we discuss below, neighboring members such as $\text{Eu}_2\text{Hf}_2\text{O}_7$ and $\text{Gd}_2\text{Hf}_2\text{O}_7$ show only a slight structural difference as measured using x-ray powder diffraction. However, very large differences between neighboring members are evident in the corresponding O-anion hopping rates as measured using PAC spectroscopy. Therefore, the application of theory to explain these large differences must meet very stringent constraints that the nature of the pyrochlore crystal structure imposes.

Several detailed reviews of the structures and properties of metal-oxide pyrochlores are available.⁴⁻⁶ We mention the more relevant properties here. In particular, the space group for the ideal pyrochlore structure is $Fd3m(O_h^7)$. A more descriptive formula is $R_2M_2O_6O'$. In this structure, all R cations are crystallographically equivalent and all M cations are equivalent. Six of the seven O anions are equivalent, and the seventh O anion has a distinct position in the structure. The structure contains eight ordered O sites per unit cell, but in each cell one of the O sites is vacant. A lattice parameter a and an "x" parameter are sufficient to describe the unit cell. The R cations, which are located within O scalenohedra, are eight coordinate, and the M cations, which are located within O trigonal antiprisms, are six coordinate.

When $x = 0.375$, the R scalenohedra become cubic and when $x = 0.3125$, the M trigonal antiprisms become perfect octahedra. In the cases of the rare-earth zirconates² and the rare-earth hafnates,⁷ the pyrochlore structure forms when $R = \text{La}, \text{Pr}, \text{Nd}, \text{Sm},$ and Gd . The $\text{Tb}_2\text{M}_2\text{O}_7$ pyrochlore may form,⁷ but the reliability of forming only the pyrochlore phase may depend on processing. For the heavier rare-earth elements $R = \text{Dy}, \dots, \text{Lu}$, the stable phase is the fluorite, in which the four R^{3+} and M^{4+} cations are distributed randomly on the fluorite cation sublattice and the seven O^{2-} anions are distributed randomly over eight equivalent O sites on the O sublattice. The pyrochlore $R_2M_2O_7$ phases are stable at laboratory temperature when the ratio of the R^{3+} ionic radius to the M^{4+} ionic radius is greater than 1.44,⁷ and when the variation reaches this value, the disordered fluorite phase becomes stable. At high temperatures some of the pyrochlore $R_2M_2O_7$ phases undergo order-disorder transitions and change to disordered fluorite phases, which occur at, for example, ≈ 1800 K for $\text{Gd}_2\text{Zr}_2\text{O}_7$.⁴ Although these transitions are, for the most part, not important to the study described here, they may provide a means to quench, either intentionally or unintentionally, a sample of either $\text{Gd}_2\text{Zr}_2\text{O}_7$ or $\text{Tb}_2\text{Zr}_2\text{O}_7$ into the disordered fluorite phase.

In nonmagnetic crystals, perturbed angular-correlation spectroscopy can be used to measure electric-field gra-

dients (EFG's) at sites into which small numbers of radioactive probe ions have been substituted. Specifically, we measure the interactions between the electric-quadrupole moment of the probe-ion nucleus and the EFG at the nucleus, which all of the electrons and other nuclei in the vicinity of the probe nucleus produce. The probe nucleus, e.g., ^{181}Hf , undergoes β decay that populates an excited level in the daughter nucleus, ^{181}Ta ; and, subsequently, two γ rays are emitted in spatially correlated directions. The emission of the first γ ray populates a relatively long-lived level, which in this case has a spin $I = \frac{5}{2}$ and a half-life $t_{1/2} = 10.8$ nsec. During the lifetime of the intermediate level, the nuclear quadrupole interaction causes the nucleus to reorient in space. Subsequently, the second γ ray is emitted into a different region of space than where it would have been emitted if no interaction had occurred. This measurable effect is the basis of PAC spectroscopy.

Measurements of static probe-site EFG's yield sharp spectral lines when each probe nucleus in the ensemble interacts with an identical EFG. This situation occurs when the probes occupy a specific site in a nearly perfect crystal. The measurements yield broadened lines when point defects lie close to the probe site and each probe in the ensemble interacts with a somewhat different EFG. When this situation occurs, a distribution of EFG's characterize the interaction. However, even an infinitely broad distribution of static EFG's does not completely destroy the angular correlation. The measurement of EFG's that fluctuate on the PAC experimental time scale, which, for the $^{181}\text{Hf} \rightarrow ^{181}\text{Ta}$ probe, varies from ≈ 0.1 to 80 nsec, yields spectral lines that show attenuation as the intermediate-level lifetime increases. An interaction with a fluctuating EFG eventually causes the destruction of the angular correlation, because the fluctuations change the direction of the quantization axis; we refer to this process as "nuclear-spin relaxation."

For convenience, we place fluctuation rates into two time-scale categories, the fast-fluctuation regime and the slow-fluctuation regime. In the fast-fluctuation regime, the fluctuation rates are much faster than the frequency that characterizes the nuclear quadrupole interaction, and the strength of the attenuation of the angular correlation *decreases* as the fluctuation rate increases. At very high fluctuation rates, the attenuation is not observable and the interaction appears to be "static." We refer to this situation as the "motional-narrowing" limit. In crystals, lattice vibrations are an example of a mechanism that causes very rapid EFG fluctuations, which generally cannot be observed. In the slow-fluctuation regime, the strength of the attenuation rate *increases* as the fluctuation rate increases. When no fluctuations occur, no attenuation of the angular correlation occurs; and the line shapes have the characteristics of static-interaction line shapes. As the rate of fluctuation increases, the lines show more and more broadening and attenuation. Depending on the relative strengths of the fluctuating and the static EFG's, the attenuation effect reaches a maximum strength at some intermediate fluctuation rate. Abragam and Pound⁸ developed the theoretical description of nuclear-spin relaxation in the fast-fluctuation-rate

regime, which is relatively easy to apply. This theory has been used to interpret PAC measurements of a variety of phenomena such as rotational motion of large molecules and complexes in solutions,⁹ hopping of oxygen anions in solids,¹⁻³ and diffusion of hydrogen in solids.^{10,11} The theoretical description of spin relaxation in the slow-fluctuation-rate regime is currently an important area of research. Blume¹² developed a stochastic model for this purpose, and Winkler and Gerdau¹³ extended this theory to analyze PAC measurements. Further refinements and applications were performed by Baudry and Boyer,¹⁴ Evenson *et al.*,¹⁵ Achtziger and Witthuhn,¹⁶ and Forker, Herz, and Simon.¹⁷ However, generally, this theory is difficult if not problematical to apply to complex spin-relaxation mechanisms in solids. Nonetheless, for some tractable cases, several investigators^{14,17} have performed comparisons between the corresponding complete theoretical treatment and the heuristic expression that experimentalists have been using, which incorporates a single attenuation factor. Generally, the results indicate that the experimentalists should continue to use these simplified equations to analyze spin-relaxation effects, especially in the fast-fluctuation-rate regime.

Generally, to interpret the result of PAC measurements, the probe chemistry must be considered. Usually the probe ion represents an impurity dopant and it differs in charge and size from the indigenous ion for which it substitutes. An important consequence is that nonindigenous probe ions may trap point defects, because the probe ions differ in charge and size from the indigenous ions. As an example, we mention the PAC measurements on CeO₂ that Wang *et al.*³ performed using the ¹¹¹In → ¹¹¹Cd probe. At low temperatures, the ¹¹¹In³⁺ probe ions trap a variety of point defects that generate probe-site EFG's, where, in this cubic crystal, the EFG's would vanish if no defects were trapped. Thus, for crystals, in which a nonindigenous probe is used to trap point defects, the PAC measurements primarily provide information about thermodynamics and kinetics that are associated with probe-defect interactions. Alternatively, when the probe ions are either indigenous or very similar in chemistry to the indigenous ion, the PAC measurements of static EFG's provide information about the local, indigenous crystal field, which may be used, for example, to understand the nature of phase transitions,¹⁸ and the PAC measurements of fluctuating EFG's provide information about the kinetics of defect transport that is not biased by interactions between nonindigenous probes and defects. The PAC measurements of static EFG's on ¹⁸¹Hf-doped R₂M₂O₇ compounds represent the case in which the probe is indigenous when M represents Hf, and they represent the case in which the probe is nearly iden-

tical to the indigenous ion in its chemistry when M represents Zr. Thus, these measurements provide information about M-site crystal fields that does not depend on chemistry differences between the native ions and the probe ions. However, the nuclear electric-quadrupole interactions take place after the ¹⁸¹Hf parent probe nucleus decays to the ¹⁸¹Ta daughter nucleus. The half-life of the ¹⁸¹Ta 615-keV level (populated by the β⁻ decay of ¹⁸¹Hf) that initiates the γ-γ cascade is approximately 18 μsec. For the measurements of O-anion transport kinetics, in which an EFG fluctuates on the experimental time scale, the probe chemistry is that of a ¹⁸¹Ta⁵⁺ ion located at either a Hf or a Zr site. As a result, the presence of a ¹⁸¹Ta⁵⁺ ion at the probe site could perturb the potential-barrier magnitude that we associate with the nuclear-spin relaxation produced by O-anion hopping.

II. EXPERIMENTAL DETAILS

Ceramic samples of the rare-earth pyrochlores R₂M₂O₇ were prepared using a resin-intermediate process. To a solution of ethylene glycol and citric acid, an aqueous solution of either ZrOCl₂ or HfOCl₂ was added. To this solution, the rare-earth was added as either a nitrate or an acetate. The ¹⁸¹Hf activity was carried by a dilute aqueous solution of HfOCl₂. The Hf carrier was added to the zirconate preparations contained Hf at < 1 at. % of the Zr concentration and Hf carrier was, therefore, insignificant as compared to the several percent of the Hf that Zr reagents usually contain. The resin was formed by heating the solution that contained the chelated metal ions. Subsequently the resin was pyrolyzed and then calcined at 1070 K. The resulting powder was pressed into small pellets and sintered in air at ≈ 1800 K for several hours. The x-ray powder diffraction patterns were measured on small amounts of powder taken from the radioactive ceramic samples on which the PAC measurements were made. The samples were generally found to be phase pure to within several percent.

A recent review presents most of the experimental details involved with performing and analyzing the PAC experiments.¹⁹ Most of the experimental time distributions were collected using a four-CsF-detector PAC spectrometer, which has a time resolution of ≈ 900 psec full width at half maximum. Simple tube furnaces were used to maintain the elevated temperatures at ± 1 K during the PAC measurements. To analyze the perturbation functions, we modified a one-site model for static nuclear-electric-quadrupole interaction that occur in a polycrystalline source to take into account the effects of calculating EFG's:

$$-A_{22}G_{22}(t_i) = A_1 \exp(-\lambda t_i) \left[S_0(\eta) + \sum_{k=1}^3 S_k(\eta) \exp(-\delta \omega_k t_i) \cos(\omega_k t_i) \right] + A_2, \quad (1)$$

in which exp(-λt_i) takes into account the attenuation of the angular correlation produced by fluctuating EFG's. Here A₁ is the normalization factor, δ is the line-shape parameter, which represents the relative width of

Lorentzian frequency distributions (of the corresponding frequency set) that give rise to static line broadening, and A₂ takes into account both the effects of γ rays that are absorbed by the sample en route to the detector and the

fraction of probe atoms that are not in a well-defined chemical environment. The site-occupancy fraction is defined as $f_1 = A_1 / (A_1 + A_2)$. The frequencies ω_k and the corresponding amplitudes $S_k(\eta)$ describe a static interaction in a polycrystalline source, and the ratio ω_2/ω_1 is used to determine the associated quadrupole frequency ω_Q and asymmetry parameter η . The nonvanishing EFG components V_{ii} in the principal-axis system where the probe nucleus is at the origin are related to the quadrupole frequency and asymmetry parameter by $\omega_Q = eQV_{zz}/4I(2I-1)\hbar$ and $\eta = (V_{xx} - V_{yy})/V_{zz}$, in which Q represents the nuclear electric-quadrupole moment (2.51b) for the spin $I = \frac{5}{2}$ intermediate quantum level in ^{181}Ta .

III. RESULTS

Figure 1 presents laboratory-temperature perturbation functions for the $R_2\text{Hf}_2\text{O}_7$ ($R = \text{La, Nd, Sm, Eu, Gd, and Tb}$) compounds. The perturbation functions for the corresponding $R_2\text{Zr}_2\text{O}_7$ ($R = \text{Nd, Sm, Eu, Gd, and Tb}$) compounds show similar features. The perturbation functions for $\text{La}_2\text{Hf}_2\text{O}_7$ and $\text{Nd}_2\text{Hf}_2\text{O}_7$ show sharp lines, and the associated frequency sets $[\omega_k, s]$ in Eq. (1) indicate that the Hf-site EFG tensor has essentially axial symmetry. Specifically $\omega_Q = 147.7 \pm 0.5 \text{ Mrad sec}^{-1}$ and $\eta = 0.07 \pm 0.02$ for $\text{La}_2\text{Hf}_2\text{O}_7$ and $\omega_Q = 181.5 \pm 0.5 \text{ Mrad sec}^{-1}$ and $\eta = 0.04 \pm 0.02$ for $\text{Nd}_2\text{Hf}_2\text{O}_7$. The M -site EFG's for these two compounds as well as for $\text{Nd}_2\text{Zr}_2\text{O}_7$ show well-defined frequencies and axial symmetry, which we would expect to observe on ordered structures that have axes of either threefold or higher rotational symmetry at the M sites.

The perturbation functions for the other compounds show varying degrees of inhomogeneous line broadening. For the $R_2\text{Hf}_2\text{O}_7$ compounds, as determined by x-ray powder diffraction, those that contain La, . . . , Tb form the pyrochlore phase, and those that contain Dy, . . . , Lu form the disordered fluorite phase. However, the Zr-containing compounds $\text{Nd}_2\text{Zr}_2\text{O}_7$, $\text{Sm}_2\text{Zr}_2\text{O}_7$, and $\text{Gd}_2\text{Zr}_2\text{O}_7$ undergo order-disorder transitions from the pyrochlore to the disordered fluorite phase at ≈ 2600 , ≈ 2270 , and $\approx 1800 \text{ K}$, respectively. Based on this information and the results of high-temperature PAC measurements on $\text{Gd}_2\text{Zr}_2\text{O}_7$ and $\text{Gd}_2\text{Hf}_2\text{O}_7$, which we discuss below, we expect the $R_2M_2O_7$ ($R = \text{Sm, Eu, and Gd}$) compounds to have pyrochlore structures in which the R^{3+} and M^{4+} cations are for the most part ordered. However, because disordered fluorite phases are accessible at high temperatures to these compounds, regions of cation disorder could exist in samples of these compounds. The compounds $\text{Tb}_2\text{Zr}_2\text{O}_7$ and $\text{Tb}_2\text{Hf}_2\text{O}_7$ could have either the pyrochlore structure or the disordered fluorite structure, or mixtures of the two. The structural details may depend strongly on the sample processing conditions. In this report, we limit our detailed measurements and analysis to the compounds that contain the rare-earth elements La, . . . , Gd.

In Fig. 1 we see that the perturbation functions for $\text{Sm}_2\text{Hf}_2\text{O}_7$, $\text{Eu}_2\text{Hf}_2\text{O}_7$, and $\text{Gd}_2\text{Hf}_2\text{O}_7$ show inhomogeneous

line broadening as do the perturbation functions for the corresponding Zr-containing compounds. To explain the origins of the line broadening, we posit an ansatz, namely, that in these compounds, the O^{2-} anions are

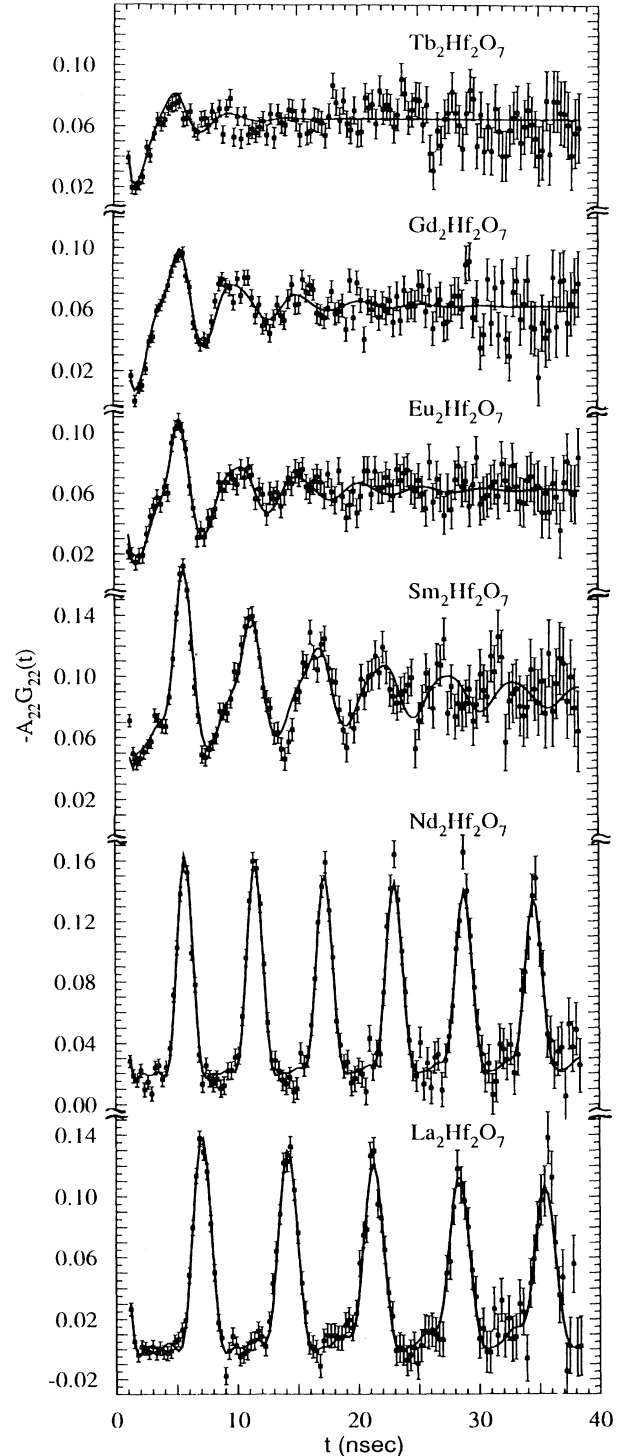


FIG. 1. Perturbation functions for the Hf-containing pyrochlores measured at laboratory temperature. The curves represent fits of Eq. (1) to the data points. The effects of static line broadening tend to increase as the rare-earth ionic radius decreases for the Sm, Eu, Gd, and Tb compounds.

disordered. Specifically, in the pyrochlore unit cell, seven out of the eight O sites are occupied. When the structure is perfectly ordered in each unit cell of the crystal, the same seven O sites are always occupied by O^{2-} ions and the eighth site is vacant. If the O^{2-} ions were sufficiently mobile, after sintering, the crystallites may form that have metastable but disordered O anions. Thus we propose that O-anion disorder causes the inhomogeneous line broadening. Now we consider the temperature dependence of the line-shape changes.

Figure 2 presents several perturbation functions that

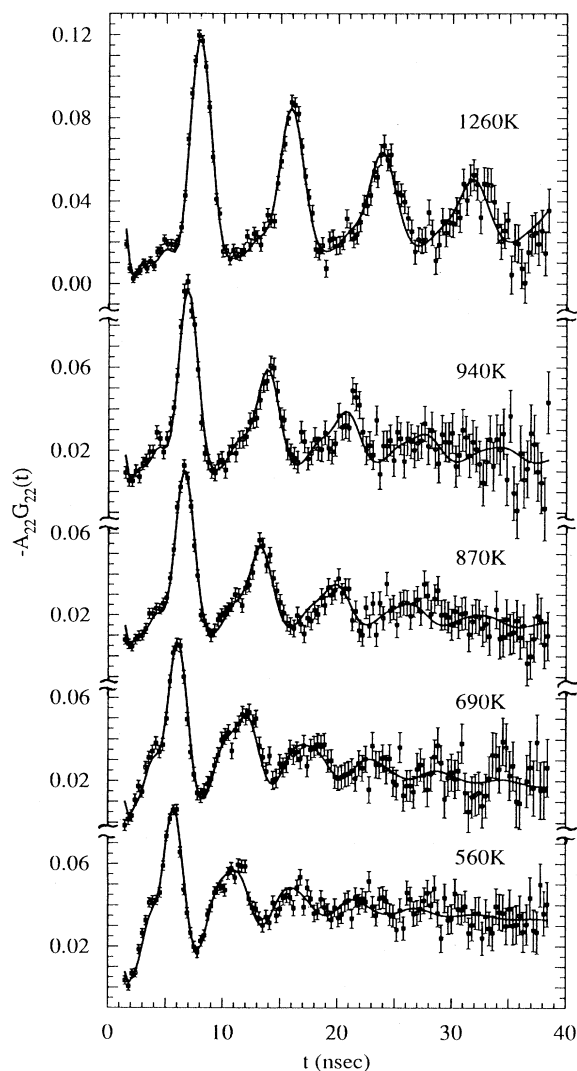


FIG. 2. Perturbation functions for a sample of the $Gd_2Zr_2O_7$ pyrochlore measured at the indicated temperatures. The curves represent fits of Eq. (1) to the data points. These perturbation functions show the effects of both line broadening, which is caused by either static effects or local disorder, and attenuation, which is caused by nuclear-spin relaxation. Although at 1260 K, the fluctuation rate has reached the motional-narrowing limit, the corresponding perturbation function shows some line broadening. This result indicates that the effects of either static defects or local disorder persist over the entire temperature range.

represent many that we measured on several samples of $Gd_2Zr_2O_7$. These perturbation functions show the effects of both inhomogeneous line broadening, which distributions of static EFG's cause, and attenuation, which fluctuating EFG's cause. The 1260-K perturbation function shows near but not complete recovery of the non-broadened line shape. When the sample reaches 1260

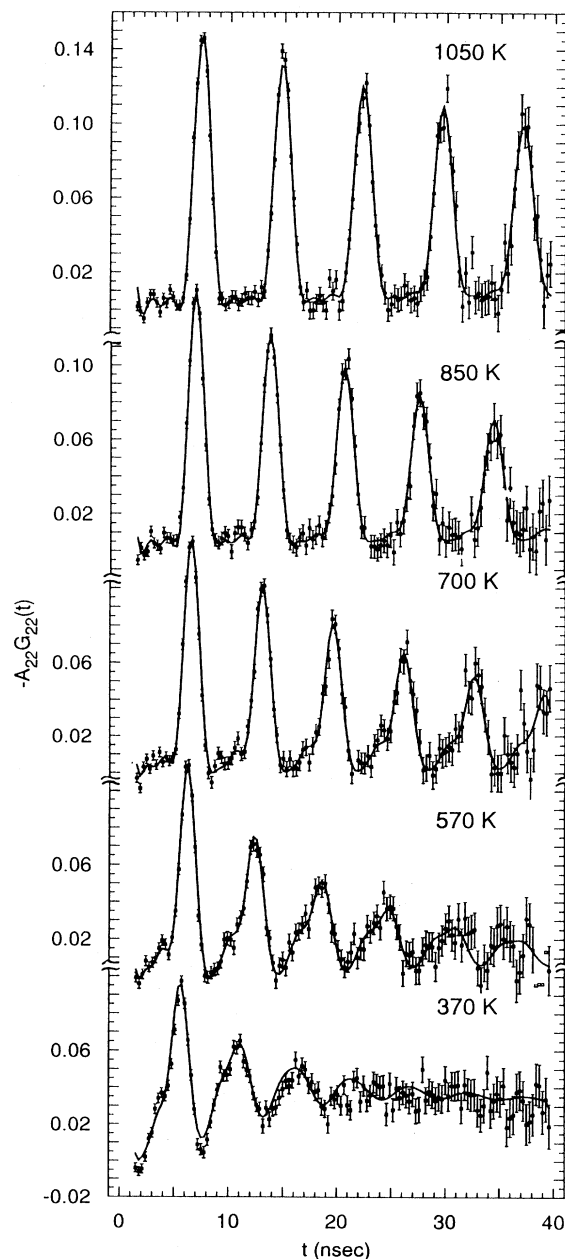


FIG. 3. Perturbation functions for a sample of the $Sm_2Zr_2O_7$ pyrochlore measured at the indicated temperatures. The curves represent fits of Eq. (1) to the data points. The 1050-K perturbation function shows very little line broadening and attenuation, and the shape of the function indicates that the corresponding time-averaged EFG has axial symmetry. This result indicates that by 1000 K the rate of the fluctuating EFG has reached the motional-narrowing limit.

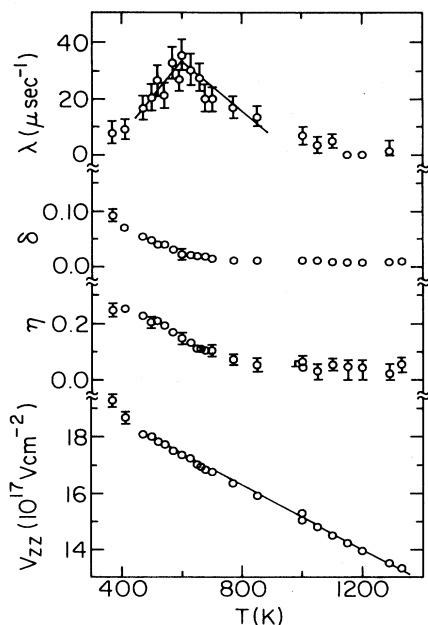


FIG. 4. Summary of parameters derived from the fits of Eq. (1) to the perturbation functions measured on a sample of $\text{Sm}_2\text{Zr}_2\text{O}_7$. The line shown on the V_{zz} temperature dependence represents a least-squares fit for $T > 400$ K that gives a slope of $-5.61 \pm 0.05 \times 10^{14} \text{V cm}^{-2} \text{K}^{-1}$ and an intercept of $20.73 \pm 0.04 \times 10^{17} \text{V cm}^{-2}$. The lines shown on the λ temperature dependences represent least-squares fits.

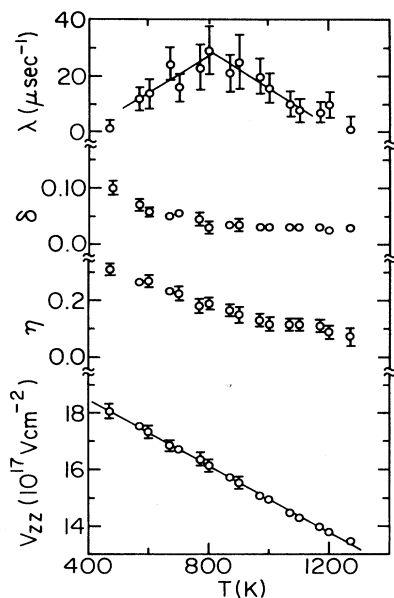


FIG. 5. Summary of parameters derived from the fits of Eq. (1) to the perturbation functions measured on a sample of $\text{Eu}_2\text{Zr}_2\text{O}_7$. The line shown on the V_{zz} temperature dependence represents a least-squares fit that gives a slope of $-5.89 \pm 0.06 \times 10^{14} \text{V cm}^{-2} \text{K}^{-1}$ and an intercept of $20.86 \pm 0.06 \times 10^{17} \text{V cm}^{-2}$. The lines shown on the λ temperature dependences represent least-squares fits.

K, the EFG fluctuation rate has already reached the motional-narrowing limit, and the effects of fluctuating EFG's are not discernible. Here we attribute the persistence of static line broadening to the effects of a small amount of cation disorder.

Figure 3 presents several perturbation functions that we measured on a sample of $\text{Sm}_2\text{Zr}_2\text{O}_7$. These perturbation functions also show the effects of both line broadening and attenuation. However, unlike the case of the 1260-K perturbation function for $\text{Gd}_2\text{Zr}_2\text{O}_7$, the 1050-K perturbation function for $\text{Sm}_2\text{Zr}_2\text{O}_7$ shows almost complete recovery of the nonbroadened line shape.

For the compounds $\text{Sm}_2\text{Zr}_2\text{O}_7$, $\text{Eu}_2\text{Zr}_2\text{O}_7$, $\text{Gd}_2\text{Zr}_2\text{O}_7$, and $\text{Gd}_2\text{Hf}_2\text{O}_7$, Figs. 4–7 present the summaries of the corresponding temperature dependences of the EFG parameters. For the compounds $\text{Sm}_2\text{Hf}_2\text{O}_7$ and $\text{Eu}_2\text{Hf}_2\text{O}_7$, the EFG parameter summaries show qualitatively similar features, except that the λ dependences on temperature are very weak. As a result, no further analysis can be performed on the parameters for these two compounds. For all of these compounds, the temperature dependence of V_{zz} is nearly linear at temperatures above 500 K. Similarly, over this range of elevated temperature, the asymmetry parameter η values and the Lorentzian line-

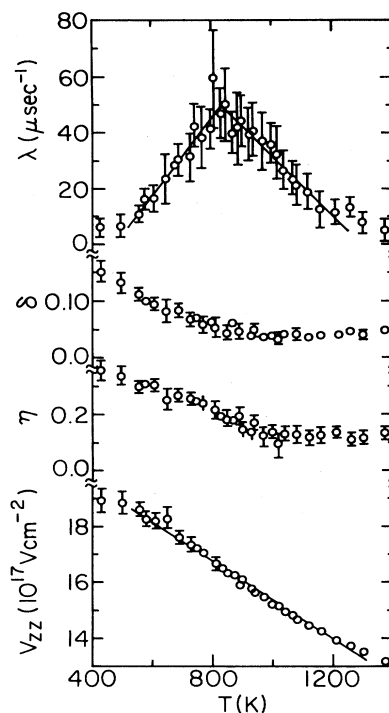


FIG. 6. Summary of parameters derived from the fits of Eq. (1) to the perturbation functions measured on a sample of $\text{Gd}_2\text{Zr}_2\text{O}_7$. The line shown on the V_{zz} temperature dependence represents a least-squares fit that gives a slope of $-7.11 \pm 0.15 \times 10^{14} \text{V cm}^{-2} \text{K}^{-1}$ and an intercept of $22.4 \pm 0.07 \times 10^{17} \text{V cm}^{-2}$. The lines shown on the λ temperature dependences represent least-squares fits. We point out that at high temperature neither δ nor λ goes to zero. Instead, some static inhomogeneous line broadening persists.

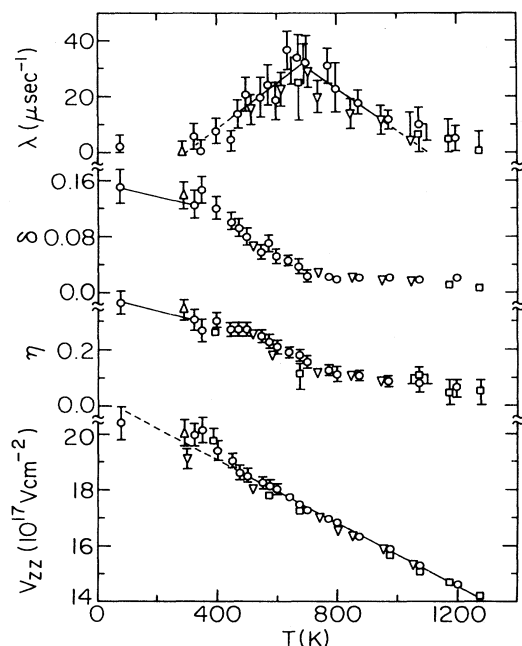


FIG. 7. Summary of parameters derived from the fits of Eq. (1) to the perturbation functions for several samples of $\text{Gd}_2\text{Hf}_2\text{O}_7$. The solid line on the V_{zz} temperature dependence represents a least-squares fit that gives a slope of $-5.64 \pm 0.08 \times 10^{14} \text{V cm}^{-2} \text{K}^{-1}$ and an intercept of $21.29 \pm 0.07 \times 10^{17} \text{V cm}^{-2}$. The lines shown on the λ temperature dependences represent least-squares fits.

shape parameter δ values tend to decrease as temperature increases. At 1200 K, except for the case of $\text{Gd}_2\text{Zr}_2\text{O}_7$, the values of η lie below 0.1 and the values of δ lie below ≈ 0.05 , and for $\text{Gd}_2\text{Zr}_2\text{O}_7$, the values of these parameters are somewhat larger. Presumably this small discrepancy arises because the $\text{Gd}_2\text{Zr}_2\text{O}_7$ compound has some inherent cation disorder that persists over the entire temperature range of interest. At temperatures below approximately 500 K, the η values and δ values increase somewhat, and the V_{zz} values deviate from linearity. These effects arise because in this temperature range, distributions of static EFG's produce most of the line broadening effects. The associated elevated δ values reflect broader distributions of EFG components that cause the asymmetry parameter values to deviate from the so-called perfect pyrochlore crystal value of zero.²⁰ These broad distributions of EFG components may cause the observed deviation of the V_{zz} values from linearity. The temperature dependences of the attenuation parameter λ values become very small and do not change much. When the attenuation effect is small, the data fitting algorithm cannot be used to select between λ and δ values uniquely. To find the temperature where the maximum λ value occurs and to find the regions where the λ value slopes increase and where they decrease, we use the empirical fact that the λ values on both sides of the maximum show a linear correlation. Thus we performed least-squares fits of the λ values to a straight line for the

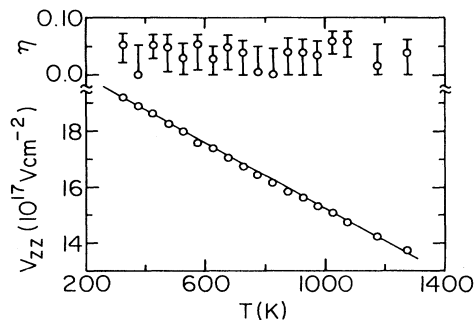


FIG. 8. Temperature dependence of V_{zz} and η derived from the fits of Eq. (1) to the perturbation functions measured on a sample of $\text{Nd}_2\text{Zr}_2\text{O}_7$. The line shown on the V_{zz} temperature dependence represents a least-squares fit that gives a slope of $-5.81 \pm 0.05 \times 10^{14} \text{V cm}^{-2} \text{K}^{-1}$ and an intercept of $21.0 \pm 0.1 \times 10^{17} \text{V cm}^{-2}$. For this series of measurements, the line-shape parameter is 0.002 ± 0.002 and the site occupancy fraction is ≈ 1.0 .

λ values on each side of the maximum. In Figs. 4–7, the fitted lines and the points used to perform the fits are evident.

Figure 8 presents the temperature dependence of V_{zz} and η measured on a sample of $\text{Nd}_2\text{Zr}_2\text{O}_7$. A linear dependence of V_{zz} on temperature and small-to-vanishing η values characterize these measurements. The absence of the deviation of V_{zz} from linearity and the lack of increases in either η or δ at lower temperature are consistent with not observing any appreciable line broadening and attenuation effects over the entire temperature range. Thus, the $\text{Nd}_2\text{Zr}_2\text{O}_7$ pyrochlore crystal appears to have ordered O anions.

IV. DISCUSSION

The analysis of the PAC measurements performed on the compounds $\text{Sm}_2\text{Zr}_2\text{O}_7$, $\text{Eu}_2\text{Zr}_2\text{O}_7$, $\text{Gd}_2\text{Zr}_2\text{O}_7$, and $\text{Gd}_2\text{Hf}_2\text{O}_7$ indicates that nuclear-spin relaxation does occur at the Zr and Hf sites in these compounds. The analysis of the measurements performed on the compounds $\text{Sm}_2\text{Hf}_2\text{O}_7$ and $\text{Eu}_2\text{Hf}_2\text{O}_7$ indicates that spin relaxation does occur but that the effect is not large enough to analyze in more detail. Therefore, we focus on the results of the former series of measurements.

In particular, we note that Eq. (1), in which an exponential attenuation factor that contains a single relaxation constant multiplies the static-interaction expression, provides a good representation of the PAC primary data. This result does not imply that the relaxation process is completely described by a single attenuation factor over the entire temperature range. Instead, we take the restricted view that the single attenuation factor $\exp(-\lambda t)$ provides a reliable representation of the relaxation process over the fast-relaxation regime. We base this viewpoint on the analysis of models of fluctuating EFG's by Forker, Herz, and Simon¹⁷ and Baudry and Boyer.¹⁴

The customary method of analysis is to consider a

thermally activated process as the cause of the spin relaxation. An O anion, for example, could jump from an occupied site to a vacant site by crossing over a potential-energy barrier. When this jump occurs near a probe ion, the EFG at the probe nucleus changes instantaneously. Thus, the rate of EFG fluctuations depends on the temperature and the barrier height ΔE , and the measured λ parameter values reflect the EFG fluctuation rate and the strength of the EFG fluctuation. Consequently, we express the dependence of the (relaxation) λ parameter on inverse temperature as

$$\lambda = \lambda_+ \exp(\Delta E_{\text{high}}/kT), \quad (2a)$$

$$\lambda = \lambda_- \exp(-\Delta E_{\text{low}}/kT). \quad (2b)$$

Here ΔE_{high} presents the activation energy for the relaxation process in the fast-relaxation higher-temperature regime, and ΔE_{low} represents the activation energy for the relaxation process in the slow-relaxation lower-temperature regime. Using Eqs. (2a) and (2b), we analyzed the measured λ parameter values. Figure 9 presents the results for $\text{Sm}_2\text{Zr}_2\text{O}_7$ and $\text{Eu}_2\text{Zr}_2\text{O}_7$, and Fig. 10 presents the results for $\text{Gd}_2\text{Zr}_2\text{O}_7$ and $\text{Gd}_2\text{Hf}_2\text{O}_7$. Using the linear plots of T versus λ , we selected the two sets of data points, one for which λ increases as T increases and one for which λ decreases as T increases. Subsequently, we fit Eqs. (2a) and (2b) to the corresponding sets of data points ($T_i^{-1}, \log \lambda_i$). Table I summarizes these results. In addition to the derived activation energies,

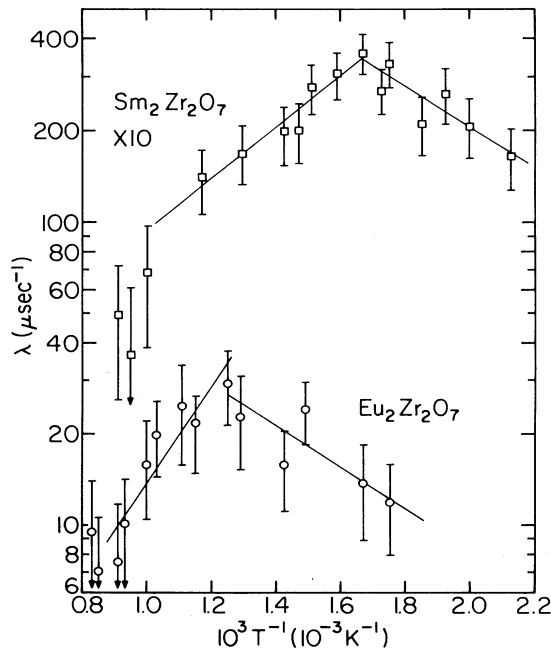


FIG. 9. Dependence of the attenuation parameter λ on inverse temperature for $\text{Sm}_2\text{Zr}_2\text{O}_7$ (for which the data point values were multiplied by 10) and for $\text{Eu}_2\text{Zr}_2\text{O}_7$. The lines represent least-squares fits of Eq. (2) to the data points. The range of inverse temperatures values included in each fit was determined by inspection of the linear plots of T versus λ .

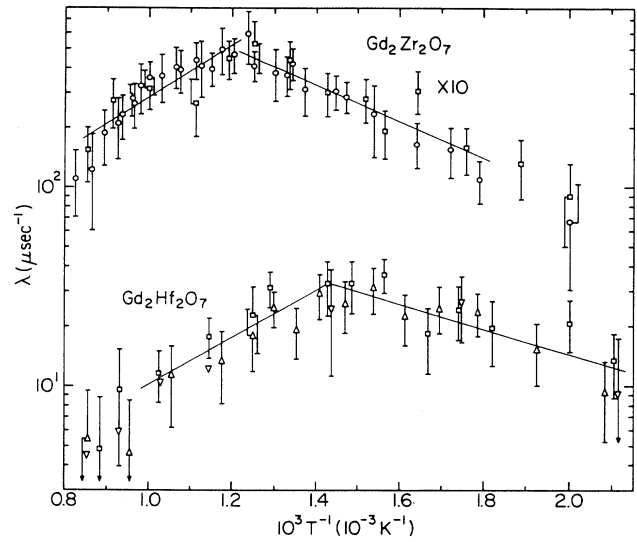


FIG. 10. Dependence of the attenuation parameter λ on inverse temperature for $\text{Gd}_2\text{Zr}_2\text{O}_7$ (for which the data point values were multiplied by 10) and for $\text{Gd}_2\text{Hf}_2\text{O}_7$. The lines represent least-squares fits of Eq. (2) to the data points. The range of inverse temperature values included in each fit was determined by inspection of the linear plots of T versus λ .

Table I presents estimates of the quadrupole frequency ω_Q^f , which are associated with the fluctuating EFG that we obtained from the results of some model calculations.^{14,17} We compare these frequencies to the corresponding quadrupole frequencies ω_Q^s for the static interaction. For the temperatures T_{cross} where the λ values are the largest, the ratio ω_Q^f/ω_Q^s ranges in value from ≈ 0.024 to ≈ 0.073 . These values indicate that the fluctuating EFG's are relatively small compared to the static EFG's. Here the relaxation effects are smaller than those observed on stabilized zirconia.^{1,2}

We identify the activation energy values ΔE_{high} , which Table I gives as the potential-energy barriers that O anions encounter when they jump from one O site to another O site. We base this identification on the ansatz that O-anion transport produces the observed spin-relaxation effects. Although the ΔE_{low} values may also represent potential-energy barriers, we consider these values to be less reliable, because they correspond to the slow-fluctuation-rate regime.¹⁷ Therefore, we focus on the physical significance of the ΔE_{high} barriers.

On ceramic samples of $\text{Nd}_2\text{Zr}_2\text{O}_7$ and $\text{Gd}_2\text{Zr}_2\text{O}_7$, Van Dijk, de Vries, and Burggraaf performed elevated-temperature electrical-conductivity measurements,²¹ which included measuring the effects of changes in the cation stoichiometry. They represent the conductivity $\sigma(T) = (\sigma_0/T) \exp(-\Delta H/RT)$, in which ΔH represents an activation enthalpy. For $\text{Nd}_2\text{Zr}_2\text{O}_7$ and $\text{Gd}_2\text{Zr}_2\text{O}_7$, they obtained preexponential factor values of $\sigma_0 \approx 2 \times 10^4 \Omega^{-1} \text{m}^{-1} \text{K}$ and $\sigma_0 \approx 2 \times 10^7 \Omega^{-1} \text{m}^{-1} \text{K}$, respectively, and activation enthalpy values of $\Delta H \approx 0.73$ – 0.78 and

TABLE I. Nuclear spin-relaxation parameters.

	Sm ₂ Zr ₂ O ₇	Eu ₂ Zr ₂ O ₇	Gd ₂ Zr ₂ O ₇	Sm ₂ Hf ₂ O ₇	Eu ₂ Hf ₂ O ₇	Gd ₂ Hf ₂ O ₇
ΔE_{high} (eV) ^a	0.17±0.02 ^c	0.32±0.06 ^c	0.25±0.03			0.24±0.03
ΔE_{low} (eV) ^a	0.13±0.03 ^c	0.14±0.04 ^c	0.19±0.01			0.12±0.02
T_{cross} (K) ^a	600±50	800±50	830±50	450±50	550±50	680±50
λ_{max} (μsec ⁻¹) ^a	35±5	25±5	50±5	12±5	25±10	34±5
ω_q^s (T_{cross}) (Mrad sec ⁻¹)	160±1	149±1	152±2	165±1	165±2	174±2
ω_Q^f (Mrad sec ⁻¹) ^b	12	8	17	4	8	11
ω_Q^f/ω_Q^s	0.073	0.066	0.11	0.024	0.051	0.065

^a T_{cross} and λ_{max} were determined using linear plots of T versus λ , and the temperature intervals used to determine ΔE_{high} and ΔE_{low} were also determined from these plots. The actual values of these energies were determined by fitting T^{-1} versus $\log\lambda$ to a straight line. T_{cross} represents the temperature where the positive-slope and the negative-slope lines intersect. λ_{max} represents the λ value at the temperature T_{max} .

^bThe quadrupole frequency corresponding to the fluctuating EFG was estimated using the relation $\lambda_{\text{max}}(\mu\text{sec}^{-1}) \approx 3\omega_Q^f$ (Mrad sec⁻¹), which was taken from Ref. 17.

^cBecause the effects of static line broadening and dynamic attenuation are difficult to separate at lower temperatures, the ΔE values may involve additional, systematic uncertainties.

0.83–0.88 eV, respectively. Here the similarity in the magnitudes of the ΔH values that correspond to the two compounds is difficult to reconcile with the corresponding difference in the preexponential factor values, which is approximately three orders of magnitude. This lack of consistency strongly suggests that the details of the electrical-conductivity mechanism may be different in the two compounds. In fact, mixed ionic and electronic conductivity has been observed in some pyrochlore compounds.²² Nonetheless, Van Dijk *et al.*²³ developed a detailed model of O-anion transport in these pyrochlores. Specifically, for both Nd₂Zr₂O₇ and Gd₂Zr₂O₇, they derive a barrier energy of approximately 0.9 eV for O-anion jumps from a 48*f* site to another 48*f* site (along either $\langle 100 \rangle$ or $\langle 110 \rangle$ directions), which they identify as the predominant kinetic pathways.²³ They conclude that their calculated barrier energy values²³ agree well with the values determined from electrical-conductivity measurements.²¹ Also, for these two compounds, they²³ suggest that differences in domain sizes could be responsible for the large differences between the corresponding σ_0 values.

The activation energy that we determined from the spin-relaxation measurements is $\Delta E_{\text{high}} = 0.25 \pm 0.03$ eV for Gd₂Zr₂O₇, and for Nd₂Zr₂O₇, we observed no spin relaxation. Therefore, these results do not agree with either the activation enthalpies that were derived from electrical-conductivity measurements²¹ or the calculated barrier heights.²³ In this context, we offer a different explanation. For Nd₂Zr₂O₇, the σ_0 value is approximately three orders of magnitude lower than the corresponding value for Gd₂Zr₂O₇. Perhaps, for Nd₂Zr₂O₇, O-anionic conductivity is not a significant mechanism. Thus, these derived enthalpy values of 0.73–0.78 eV (Ref. 21) are an artifact of whatever type of conductivity was measured. For Gd₂Zr₂O₇, O-anionic conductivity may be operative, but this type of conductivity may involve different potential-energy barriers, which, for example, could occur near grain boundaries; hence, the discrepancy be-

tween $\Delta E_{\text{high}} = 0.25$ eV, measured by PAC spectroscopy, and $\Delta H \approx 0.73$ –0.78 eV, derived from conductivity measurements, could arise because two different phenomena have been observed. Moreover, the apparent agreement between the model-derived barrier of 0.9 eV (Ref. 23) and the conductivity results could be fortuitous. The null result that we observed on Nd₂Zr₂O₇ and the large spin relaxation that we observed on Gd₂Zr₂O₇ indicate clearly that subtle structural differences between the two crystals prevent O-anion transport from taking place in Gd₂Zr₂O₇ and allow it to take place in Gd₂Zr₂O₇. The model,²³ on the other hand, yields essentially the same barrier energy for both compounds. Therefore, we conclude inexorably that neither the conductivity measurement nor the model calculations provide a good representation of O-anion transport in these pyrochlore crystals.

V. CONCLUSIONS

Using the ¹⁸¹Hf→¹⁸¹Ta PAC probe, we have measured static and fluctuating EFG's at the *M* sites in *R*₂*M*₂O₇ pyrochlore ceramics. For the Nd₂Zr₂O₇ compound over the entire temperature range, we observed static, axially symmetric nuclear electric-quadrupole interactions that sharp spectral lines characterize. For the Sm₂Hf₂O₇ and Eu₂Zr₂O₇ compounds, we observed the effects of relatively weak nuclear-spin relaxation, which we did not analyze in detail. For the Sm₂Zr₂O₇, Eu₂Zr₂O₇, Gd₂Zr₂O₇, and Gd₂Hf₂O₇ compounds, we observed strong spin-relaxation effects, and, using the measured attenuation parameters that correspond to the fast-relaxation-rate regime, we derived activation energies that range from 0.17 to 0.32 eV. We attribute these activation energies to the potential-energy barriers that O anions encounter when they jump from an occupied O site to a vacant O site in the cation-ordered pyrochlore structure. These activation energies do not agree either with activation enthalpy values that were derived from electrical-conductivity measurements²¹ or with model calculations performed for

the $Nd_2Zr_2O_7$ and $Gd_2Zr_2O_7$ compounds.²³ For these pyrochlore crystals, the conductivity measurements do not provide sufficiently unique information to give reliable activation energies that correspond to a specific kinetic pathway in the structure such as a $48f$ to $48f$ O-anion jump. The model calculations, for reasons that are not clear to us, also do not provide a good representation of the O-anion kinetics. Therefore, the activation energies that we derive from the PAC measurements of spin relaxation provide an important benchmark for theoretical models of O-anion transport in these pyrochlore crystals.

ACKNOWLEDGMENTS

We greatly appreciate the insights and critical comments that Professor Darrell G. Schlom at Pennsylvania State University, Professor Manfred Forker at Institut für Strahlen- und Kernphysik der Universität Bonn, and Professor William E. Evenson of Brigham Young University have given to us. We thank the Office of Naval Research for providing partial support via Grant No. N00014-90-J4112. We thank the Radiation Science and Engineering Center of Pennsylvania State University for producing the ^{181}Hf isotope.

-
- ¹A. Baudry, P. Boyer, and A. L. deOliveira, *J. Phys. Chem. Solids* **43**, 871 (1982).
- ²J. A. Gardner, H. Jaeger, H. T. Su, W. H. Warnes, and J. C. Haygarth, *Physica B* **150**, 223 (1988), and references therein.
- ³R. Wang, J. A. Gardner, W. E. Evenson, and J. A. Sommers, *Phys. Rev. B* **47**, 638 (1993).
- ⁴M. A. Subramanian, G. Avramudan, and G. V. Subba Rao, *Prog. Solid State Chem.* **15**, 55 (1983).
- ⁵G. Albanese, A. Deriu, J. E. Greedan, M. S. Seehra, K. Sirtori, and H. P. J. Wijn, in *Properties of Non-Metallic Inorganic Compounds Based on Transition Elements*, Vol. 27 of Landolt-Börnstein, Group III: Crystal and Solid State Physics, edited by H. P. J. Wijn (Springer-Verlag, Heidelberg, 1992), pp. 100–123.
- ⁶M. A. Subramanian and A. W. Sleight, in *Handbook on the Physics and Chemistry of Rare Earths*, edited by K. A. Gschneider, Jr., and L. Eyring (Elsevier, Amsterdam, 1993), Chap. 107, pp. 225–248.
- ⁷L. H. Brixner, *Mater. Res. Bull.* **19**, 143 (1984).
- ⁸A. Abragam and R. V. Pound, *Phys. Rev.* **92**, 943 (1953).
- ⁹See, for example, J. S. Barrett, J. A. Cameron, P. R. Gardner, L. Keszthelyi, W. V. Prestwich, and M. Kaplan, *J. Chem. Phys.* **53**, 759 (1970).
- ¹⁰R. Heidinger, P. Peretto, and S. Choulet, *Solid State Commun.* **47**, 283 (1983).
- ¹¹H. C. Jain, L. Freise, and M. Forker, *J. Phys. Condens. Matter* **1**, 2157 (1989).
- ¹²M. Blume, *Phys. Rev.* **174**, 351 (1968).
- ¹³H. Winkler and E. Gerdau, *Z. Phys.* **267**, 363 (1973).
- ¹⁴A. Baudry and P. Boyer, *Hyperfine Interact.* **35**, 803 (1987).
- ¹⁵W. E. Evenson, J. A. Gardner, R. Wang, and A. G. McKale, *Hyperfine Interact.* **62**, 283 (1990).
- ¹⁶A. Achtziger and W. Witthuhn, *Phys. Rev. B* **47**, 6990 (1973).
- ¹⁷M. Forker, W. Herz, and D. Simon, *Nucl. Instrum. Methods Phys. Res. Sec. A* **337**, 534 (1994).
- ¹⁸See, for example, G. L. Catchen and D. M. Spaar, *Phys. Rev. B* **44**, 12 137 (1991); G. L. Catchen, T. M. Rearick, E. F. Hollinger, D. W. Esh, and J. M. Adams, *Ferroelectrics* **156**, 239 (1994); G. L. Catchen, T. M. Rearick, and D. G. Schlom, *Phys. Rev. B* **49**, 318 (1994).
- ¹⁹G. L. Catchen, *J. Mater. Edu.* **12**, 253 (1990).
- ²⁰M. Forker, *Nucl. Instrum. Methods* **106**, 121 (1973).
- ²¹T. Van Dijk, K. J. deVries, and J. J. Burggraaf, *Phys. Status Solidi A* **58**, 115 (1980).
- ²²H. L. Tuller, *Solid State Ionics* **52**, 135 (1992).
- ²³M. P. Van Dijk, A. J. Burggraaf, A. N. Cormack, and C. R. A. Catlow, *Solid State Ionics* **17**, 159 (1985).